Ultrasonics - Sonochemistry 59 (2019) 104757

Contents lists available at ScienceDirect

Ultrasonics - Sonochemistry

journal homepage: www.elsevier.com/locate/ultson

$Ni_{0.4}Cu_{0.2}Zn_{0.4}Tb_xFe_{2-x}O_4$ nanospinel ferrites: Ultrasonic synthesis and physical properties

Y. Slimani[a,*], M.A. Almessiere[a,b], A. Demir Korkmaz[c], S. Guner[d], H. Güngüneş[e], M. Sertkol[f], A. Manikandan[g], A. Yildiz[h], S. Akhtar[a], Sagar E. Shirsath[i], A. Baykal[j]

[a] Department of Biophysics, Institute for Research and Medical Consultations (IRMC), Imam Abdulrahman Bin Faisal University, P.O. Box 1982, 31441 Dammam, Saudi Arabia
[b] Department of Physics, College of Science, Imam Abdulrahman Bin Faisal University, P.O. Box 1982, 31441 Dammam, Saudi Arabia
[c] Department of Chemistry, Istanbul Medeniyet University, 34700 Istanbul, Uskudar, Turkey
[d] Institute of Inorganic Chemistry, RWTH Aachen University, D-52074 Aachen, Germany
[e] Department of Physics, Hitit University, 19030 Çevre Yolu Bulvarı-Çorum, Turkey
[f] Deanship of Preparatory Year Building 450, Imam Abdulrahman Bin Faisal University, P.O. Box 1982, 31441 Dammam, Saudi Arabia
[g] Department of Chemistry, Bharath Institute of Higher Education and Research (BIHER), Bharath University, Chennai 600073, Tamil Nadu, India
[h] Department of Textile Engineering, Namık Kemal University, 59860 Corlu-Tekirdag, Turkey
[i] School of Materials Science and Engineering, University of New South Wales, Kensington, Sydney, NSW 2052, Australia
[j] Department of Nanomedicine Research, Institute for Research and Medical Consultations (IRMC), Imam Abdulrahman Bin Faisal University, P.O. Box 1982, 31441 Dammam, Saudi Arabia

ARTICLE INFO

Keywords:
Magnetic nanomaterials
Rare earth substitution
Structure
Optical properties
Magnetic properties
Cation distribution

ABSTRACT

The Fe^{3+} ions were replace with Tb^{3+} ions as highly paramagnetic rare earth element within the structure of $Ni_{0.4}Cu_{0.2}Zn_{0.4}Fe_2O_4$ nano-spinel ferrites (NSFs). The structural, magnetic, spectroscopic and optic properties have been studied in details. All products have been synthesized via ultrasonic approach via Qsonica ultrasonic homogenizer, frequency: 20 kHz and power: 70 W for 60 min. No annealing or calcination process was applied for any product. The microstructural analysis of products has been done via X-ray powder diffractometry (XRD) which presented the cubic spinel structure with nanosized distribution of all. The cubic morphology of all products were confirmed by both HR-TEM and FE-SEM. Optical band gap (E_g) values were assessed by applying %DR (percent diffuse reflectance) analysis and Kubelka-Munk theory. The Tauc schemes showed that E_g values are in a narrow range (1.87–1.98 eV). The quadrupole splitting, line width, hyperfine magnetic field, isomer shift values and cation distribution have been determined from ^{57}Fe Mossbauer analysis. The magnetic properties of various nanoparticles have been obtained from VSM (vibration sample magnetometer) measurements at 10 and 300 K (RT). The magnetic results revealed superparamagnetic and soft ferromagnetic traits at 10 and 300 K, respectively. M_s (saturation magnetization) and M_r (remanence) initially increase with increasing Tb^{3+} substituting level up to x = 0.06 then diminish for further x values. H_c (coercivity) shows an opposite variation tendency of M_s and M_r. The observed magnetic traits are deeply discussed in relation with the structure, morphology, magnetic moments and cation distributions.

1. Introduction

Magnetic nanoparticles (MNPs) have concerned significant interest in for the last 50 years because of their superparamagnetic characteristics, high surface-to-volume ratio, etc [1,2]. Among all magnetic nanomaterials, spinel ferrites have distinguishable magnetic, electrical and optic properties [3–5]. Their magnetic and electrical properties such as high saturation magnetization (M_s) as well as high dielectric properties, low eddy current loss, initial permeability enable a wide range of applications for spinel ferrites [6]. A considerable amount of applications of ferrite nanoparticles exists including biomedical imaging as MRI contrast agents [7,8], drug delivery [9–11], magnetic hyperthermia [12,13], catalysis [14], gas sensing [15], electromagnetic interference (EMI) shielding [16], high-frequency antennas [17], isolators [18], circulators [19], phase shifters [20], multilayer chip inductors (MLCIs) [21], etc. The electrical, optical and magnetic traits of ferrites could be adjusted by altering the formula by substituting the ions in the formula with different ions or by the introduction of

* Corresponding author.
E-mail address: yaslimani@iau.edu.sa (Y. Slimani).

https://doi.org/10.1016/j.ultsonch.2019.104757
Received 22 July 2019; Received in revised form 26 August 2019; Accepted 27 August 2019
Available online 27 August 2019
1350-4177/

additives to obtain novel materials for those applications [22,23]. Several efforts have been made to examine the substitution of metal ions in ferrites with numerous metal ions [24,25]. However, the number of studies conducted to examine the consequence of trivalent rare earth metal ions (RE^{3+}) on the possessions of spinel ferrites is limited [26–30]. These studies have shown that doping spinel ferrites with RE^{3+}, which display paramagnetic behavior in the molecular environment, results in superior magnetic characteristics and good surface morphology [31]. The large ionic radius of RE^{3+} elements as compared with that of Fe^{3+} causes a micro-strain, which results in the distortion of the spinel ferrite's building [32]. This, consecutively, leads to an improvement in magnetic characteristics [26,27].

Nickel copper zinc ferrite (NCZF) is an important magnetic material mostly required in technological applications such as MLCIs with its superior characteristics: high permeability, large electrical resistivity, and low sintering temperature [33]. MLCIs are used in numerous electronic circuits to support in reducing the size of numerous communication and other electronic devices such as video cameras, mobile phones and notebook computers. Researchers have reported many papers about the synthesis of nickel copper zinc ferrites. For example, Reddy et al. [34] synthesized nickel copper zinc ferrites by microwave sintering technique for MLCI applications. They have found that M_s, dielectric loss, dielectric constant, and the permeability of the ferrites decreased as the Zn was replaced by Ni. Another study by Gabal et al. [35] examined the magnetic, electrical and structural characteristics of La^{3+} substituted NCZF fabricated by freshly extracted egg white and metal nitrates. They concluded that the increase in La^{3+} substitution resulted in reducing the particle size and bulk density, and increasing the lattice constant, size-dependent coercivity, and a decrease in Curie temperature. Shrotri and co-workers [36] reported the incorporation of copper to nickel zinc ferrite with a formula $Ni_{0.8-x}Cu_xZn_{0.2}Fe_2O_4$ (x = 0–0.4) prepared by co-precipitation method. The ferrites showed a single phase between x = 0.0 and 0.2 while above x = 0.2, secondary phases of copper oxide were observed. The composition with x = 0.2, $Ni_{0.6}Cu_{0.2}Zn_{0.2}Fe_2O_4$, displayed the highest density (5.02 g/cm^3) with a large grain size and low number of pores resulting in the highest resistivity (7.3 × 107 O.cm) as well as a decline in the demagnetizing field and an enhanced in the permeability [36]. Hsiang et al. [37] applied a solid-state method to prepare NCZFs with the formula $Ni_{0.42}Zn_{0.45}Cu_{0.13+x}Fe_{2-x}O_4$ ($x \leq 0.1$). Again, the samples exhibited a single phase in XRD patterns up to x = 0.07, where the molar ratio of copper was 0.2, and above this composition a secondary phase occurred. Moreover, the composition x = 0.07 displayed a very good initial permeability ($\mu 325 = '$) and excellent DC-superposition properties, which can improve the productivity of circuit systems. Therefore, it is feasible to set the molar ratio of copper ion as 0.2 in the composition of a NCZF sample.

There are many techniques for synthesizing nickel copper zinc ferrite nanoparticles such as co-precipitation, citrate assisted auto-combustion, hydrothermal, reverse micelle, microwave synthesis, sol-gel, and ultrasonication [38,39].

One of the mentioned techniques, ultrasonic is an efficient physical methods to establish the homogenies dispersed phase, lessen particles size and deagglomeration of particles for improving the uniformity and stability. Ultrasonication is streamlined method to get high-purity materials. Moreover, this technique characterized in that consume-less products, saving time and improved the reaction rate. The sonochemical reaction was performed by pressure using amplitude shock wave produced by the cavitation. At the end of the reaction, local 'hot spots' with a generation of high local temperature has been created due to high number of collisions between the reactants [29]. The preparation of NCZF with sonochemistry has advantages in comparison to other methods including avoiding the agglomeration of nanoparticles, crystal size distribution control, decrease of the induction time, growth in the amount of crystals at equivalent supersaturation, and avoiding excess amounts of organic solvents to contribute to green chemistry [29].

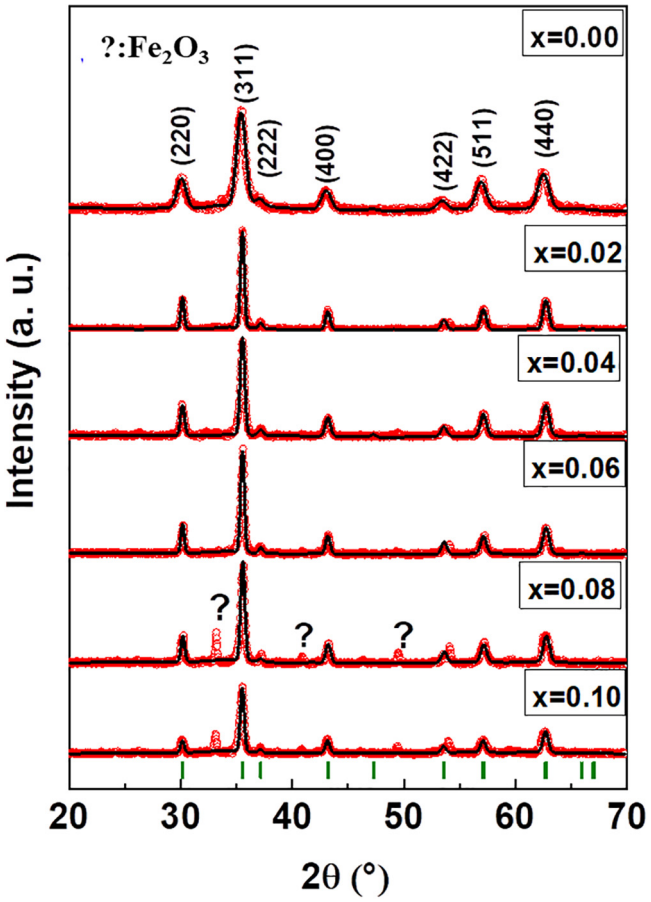

Fig. 1. XRD powder patterns of $Ni_{0.4}Cu_{0.2}Zn_{0.4}Tb_xFe_{2-x}O_4$ (x = 0.00–0.10) NSFs.

Table 1
Tb content, refined structural parameters for $Ni_{0.4}Cu_{0.2}Zn_{0.4}Tb_xFe_{2-x}O_4$ (x = 0.00–0.10) NFSs.

x	a (Å)	V (Å)^3	D_{XRD}(nm) ± 0.08	$\chi^2(chi^2)$	R_{Bragg}
0.00	8.370(0)	586.37	12.40	1.36	2.73
0.02	8.371(7)	586.74	16.16	2.17	3.47
0.04	8.375(0)	587.42	18.30	1.93	3.07
0.06	8.383(4)	589.18	19.37	1.99	2.80
0.08	8.384(2)	589.36	19.34	2.86	5.85
0.10	8.389(3)	590.43	18.71	2.59	6.01

In this particular study, we described the fabrication of $Ni_{0.4}Cu_{0.2}Zn_{0.4}Tb_xFe_{2-x}O_4$ (x = 0.00–0.10) NSFs fabricated via sonochemical approach. The structural and various physical characteristics of these products were investigated.

2. Experimental

The sonochemical method was employed to fabricate $Ni_{0.4}Cu_{0.2}Zn_{0.4}Tb_xFe_{2-x}O_4$ (x = 0.00–0.10) NSFs. Nickel(II) nitrate hexahydrate, Zinc nitrate hexahydrate, copper nitrate trihydrate, iron (III) nitrate nonahydrate and terbium oxide were utilized as the starting materials. A specific amount of salt nitrite was dissolved in deionized (DI) water, which formed the first solution. The second solution consists of Tb_4O_7 thawed in 12 ml of conc. HCl at 180 °C. Then two solutions containing metal salts were mixed and the pH was adjusted to 11 with 2 M of NaOH then the resultant solution was irradiated with ultrasonic irradiation (UZ SONOPULS HD 2070 Ultrasonic Homogenizer with 20 kHz and 70 W) for half an hour. Finally, magnetic product was

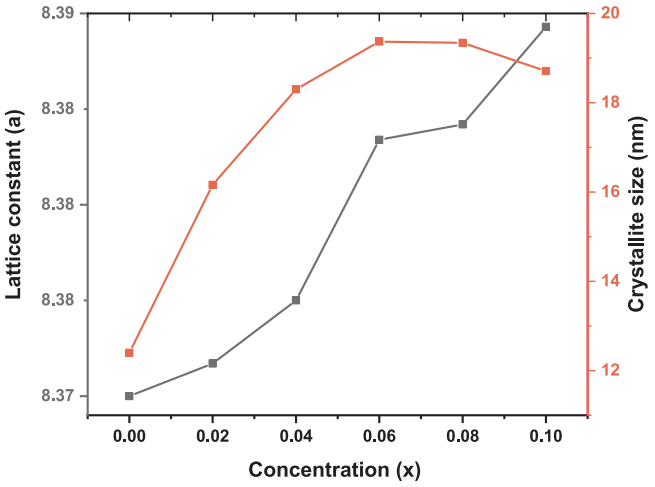

Fig. 2. Lattice constant **(a)** and crystallite size (nm) as function of "x".

washed with DI water then dried at 75 °C.

Microstructural analysis samples were done by Rigaku Benchtop Miniflex X-ray diffraction (XRD, CuK_{α} radiation). A scanning electron microscope (SEM; FEI Titan ST) with an EDX (energy dispersive X-ray) spectrometer system was utilized for the surface morphology and chemical compositions. FEI Morgagni 268A transmission electron microscopy (TEM) was utilized for the morphological investigations. Room temperature Mossbauer analyses were done MagLab Mossbauer instrument. Bruker Fourier-transform infrared (FT-IR) spectrophotometer was used for the spectral analysis (4000–400 cm^{-1}). The SQUID from Quantum Design coupled with VSM head (vibrating sample magnetometer) was employed for magnetic investigations.

3. Results and discussion

3.1. Structure

X-ray diffraction patterns of of $Ni_{0.4}Cu_{0.2}Zn_{0.4}Tb_xFe_{2-x}O_4$ (x = 0.00–0.10) NSFs have been displayed in Fig. 1. The XRD powder patterns were given in Fig. 1 which has a good agreement with ICDD card of spinel structure 10-0325. The Rietveld refinement by Match3! and full proof program was employed to calculate the average crystallite sizes and lattice constants given in Table 1. The observed hkl values; (2 2 0), (3 1 1), (2 2 2), (4 0 0), (4 2 2), (5 1 1) and (4 4 0), match well with the ICDD card no: 10-0325 of $NiFe_2O_4$. It was observed that

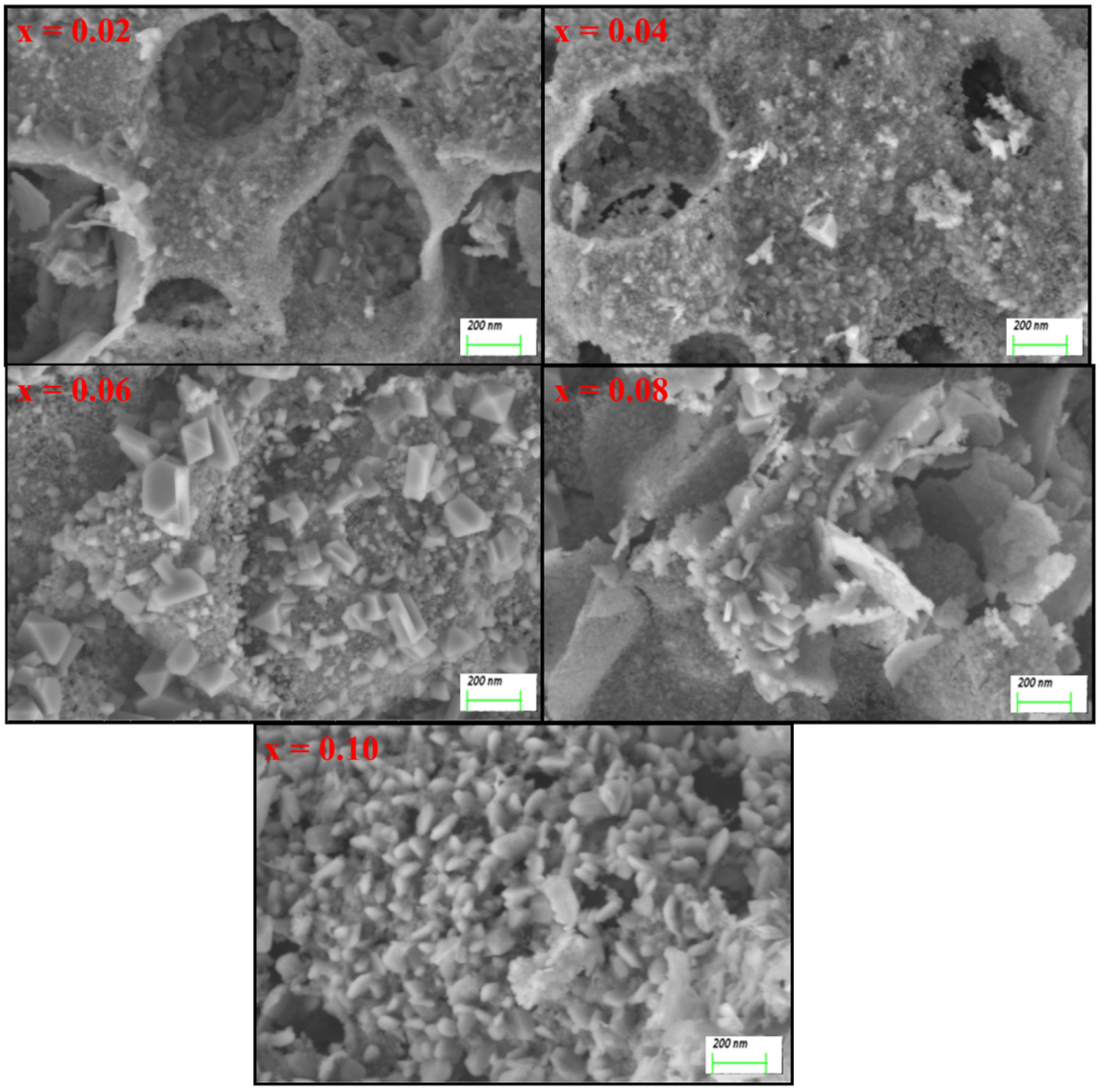

Fig. 3. SEM images of $Ni_{0.4}Cu_{0.2}Zn_{0.4}Tb_xFe_{2-x}O_4$ (x = 0.02–0.10) NSFs.

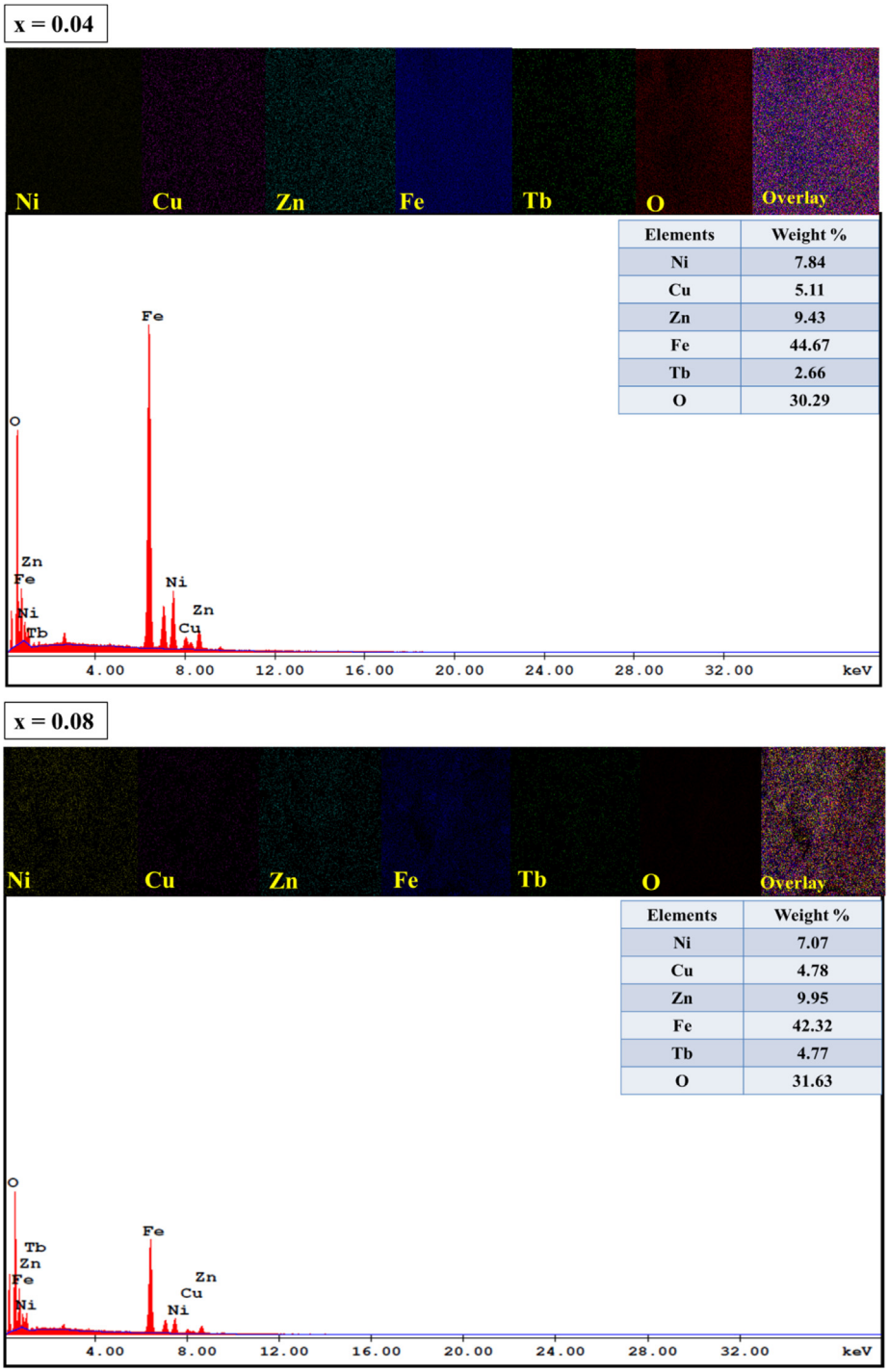

Fig. 4. EDX and elemental mapping of $Ni_{0.4}Cu_{0.2}Zn_{0.4}Tb_xFe_{2-x}O_4$ (x = 0.04 and 0.08) NSFs.

there is minor impurity for x = 0.08 and 0.1 samples as secondary phase was identified as α-Fe_2O_3 with ICDD 33-0664. Due to the solubility limit (called as limit of substitution), this impurity phase and possible lattice distortion maybe produced [40,41]. Actually Fe^{3+} ions can NOT be substituted completely larger Tb^{3+} ions. Hence, the secondary phases (α-Fe_2O_3 or $TbFeO_3$) may form at grain boundaries and due to interactions of ions with each other. The rare earth ions substitution causes somehow distortions in O_h and T_d sites of lattice due to that the r_{Tb}^{3+} of Tb^{3+} ions (1.06 Å) are larger than that of r_{Fe}^{3+} (0.67 Å) [42]. Therefore, lattice parameter 'a_o' of $Ni_{0.4}Cu_{0.2}Zn_{0.4}Tb_xFe_{2-x}O_4$ NSFs is increased with increasing the Tb ratio [43,44] to a certain extent. Hence it is found that the average crystal sizes are increased with rising the Tb ratio until x = 0.06 then diminished marginally with further increasing Tb concentration owing to the formation of α-Fe_2O_3 as secondary phase which may prevent the crystal growth. The estimated D_{XRD} were presented in in Fig. 2.

3.2. Microstructure analysis

Fig. 3 depicted the SEM micrographs of $Ni_{0.4}Cu_{0.2}Zn_{0.4}Tb_xFe_{2-x}O_4$ (x = 0.00–0.10) NSFs. The ferrite compositions has an aggregation of small cubic grains. The grains shape gradually converted for taking a cubic shape to be more uniform with increasing Tb content. EDX spectra and elemental mapping are endorsed the consistent elements of

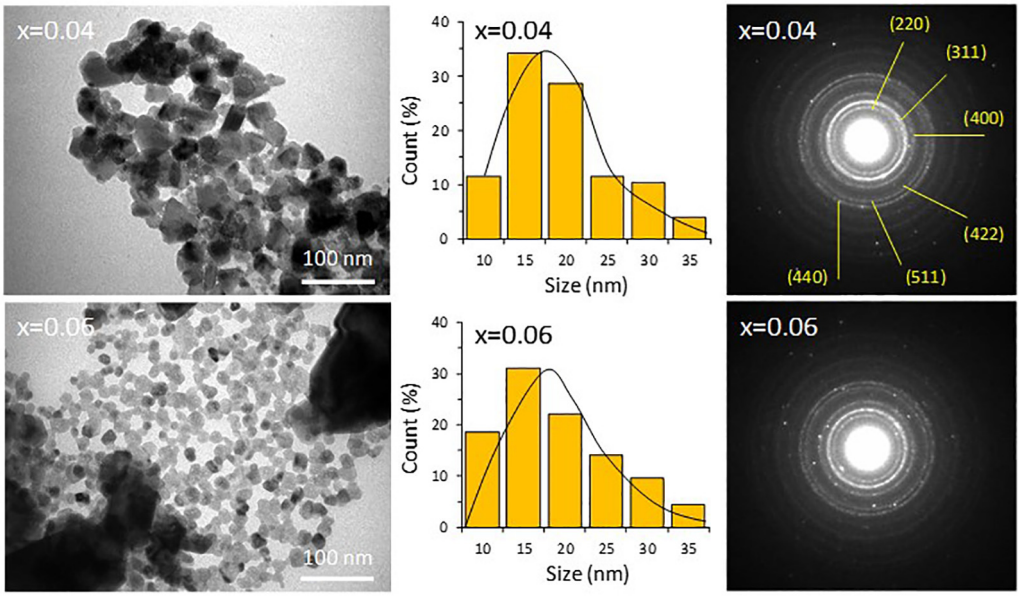

Fig. 5. TEM images, histograms and selected area electron diffraction (SAED) patterns of $Ni_{0.4}Cu_{0.2}Zn_{0.4}Tb_xFe_{2-x}O_4$ (x = 0.04 and 0.06) NSFs.

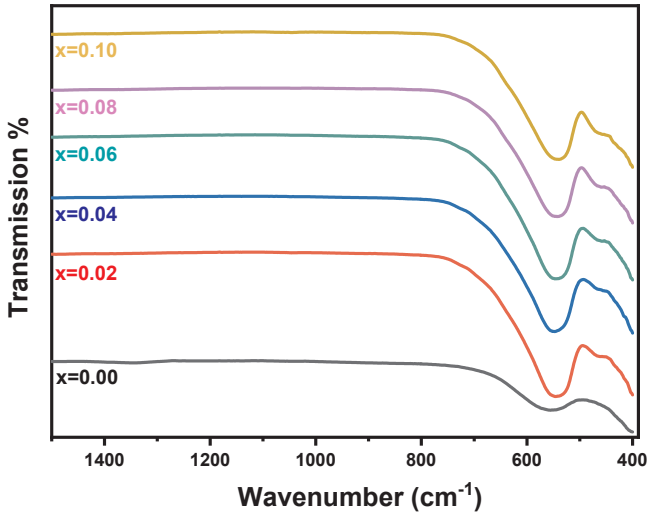

Fig. 6. FT-IR spectra of $Ni_{0.4}Cu_{0.2}Zn_{0.4}Tb_xFe_{2-x}O_4$ (x = 0.00–0.10) NSFs.

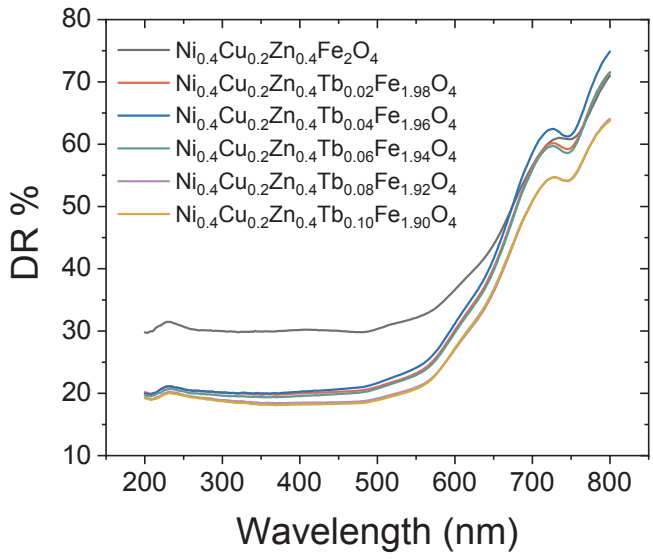

Fig. 7. DR % spectra of $Ni_{0.4}Cu_{0.2}Zn_{0.4}Tb_xFe_{2-x}O_4$ (x = 0.00–0.10) NSFs in the near UV–Visible region.

prepared $Ni_{0.4}Cu_{0.2}Zn_{0.4}Tb_xFe_{2-x}O_4$ (x = 0.04 and 0.08) NSFs as shown in Fig. 4. All the EDX peaks are matched to Cu, Ni, Zn, Fe, Tb, and O elements. The size and structure of $Ni_{0.4}Cu_{0.2}Zn_{0.4}Tb_xFe_{2-x}O_4$ (x = 0.04 and 0.06) NSFs were investigated further by TEM as recorded in Fig. 5 which presented the cubic morphology.

3.3. Bonding

FT-IR spectra of $Ni_{0.4}Cu_{0.2}Zn_{0.4}Tb_xFe_{2-x}O_4$ (x = 0.00–0.10) NSFs have been displayed in Fig. 6. All compositions presented FT-IR stretching bands at 581 and 410 cm^{-1} (due to Me-O stretching) [27]. It has been noted that the substitution of the Tb^{3+} ions into the $Ni_{0.4}Cu_{0.2}Zn_{0.4}Fe_2O_4$ NSFs has to some extent shifted peaks in the direction of higher frequency side. This shifting indicates the micro-strain in the $Ni_{0.4}Cu_{0.2}Zn_{0.4}Fe_2O_4$ NSFs lattices caused by the larger size of substituting Tb^{3+} ions and the change in the distance of iron oxygen bond [28].

3.4. Optic analysis

Optoelectronic properties of $Ni_{0.4}Cu_{0.2}Zn_{0.4}Tb_xFe_{2-x}O_4$ (x = 0.00–0.10) NSFs were examined by DR % (percent diffuse reflectance) measurements within 200–800 nm range (Fig. 7). The %DR spectra for substituted samples exhibit in a narrow band of 18%–23% in sweep interval of 200 nm-570 nm. In the same region, pristine $Ni_{0.4}Cu_{0.2}Zn_{0.4}Fe_2O_4$ NSFs has reflectance value around 30%. There is almost a linear increase except around 745 nm at reflectance values at all spectra until maximum 75% in the rest sweep range between 570 and 800 nm. The interpretation of DR % spectra is based on the Kubelka-Munk theory. $F(R_\infty)$ denotes the Kubelka-Munk function:

$$F(R_\infty) = \frac{(1-R_\infty)^2}{2R_\infty} = \frac{2.303\varepsilon C}{S} = \alpha \quad (1)$$

In equation, absoluteremittanceR_∞, absorptivity ε, the analyte concentration C, and the scattering coefficient S represent the absorption coefficient α. Optical band gap (E_g) of the NSFs are estimated using T_{auc}

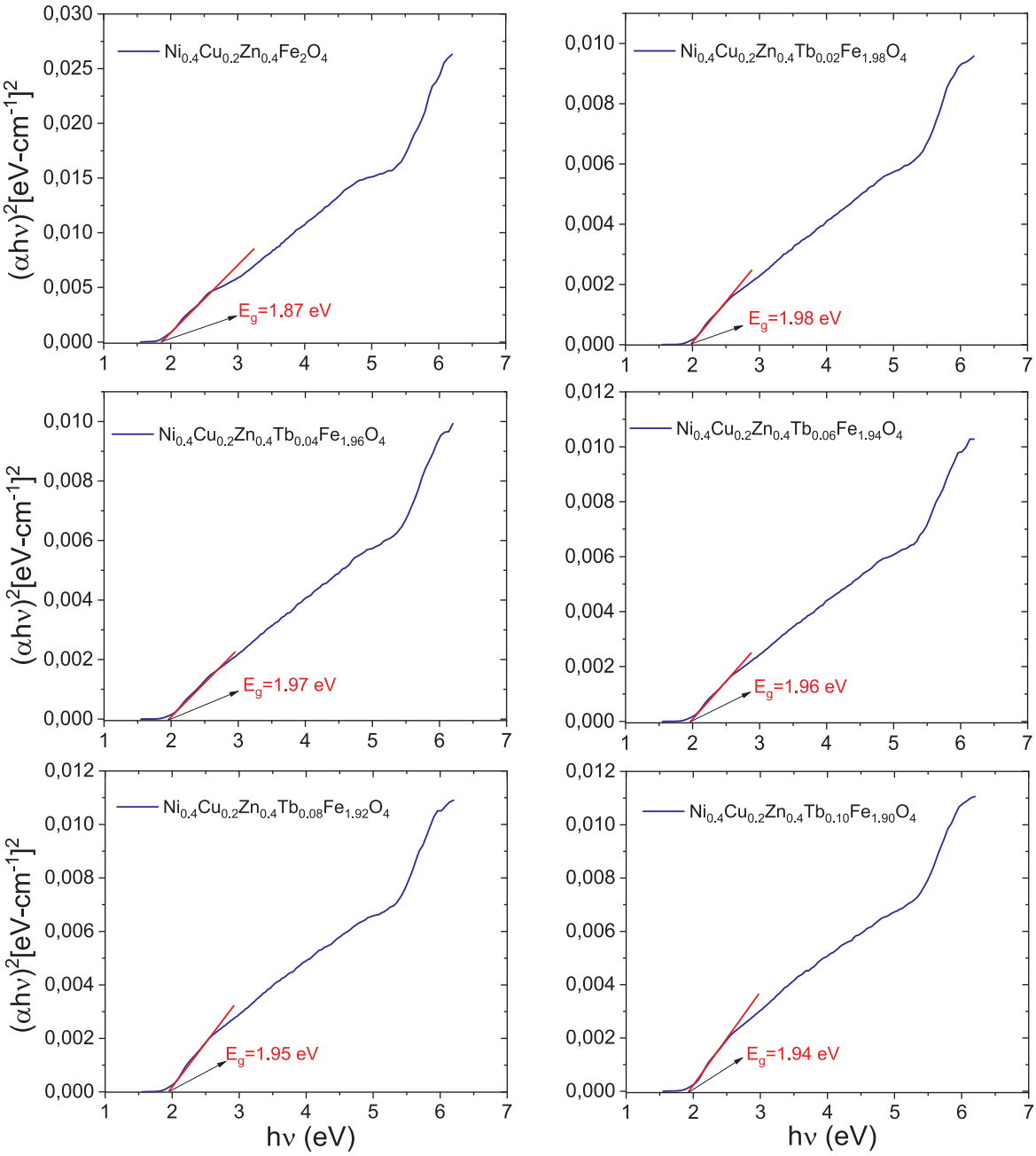

Fig. 8. Tauc plots of $Ni_{0.4}Cu_{0.2}Zn_{0.4}Tb_xFe_{2-x}O_4$ (x = 0.00–0.10) NSFs. Extrapolating the straight portion of graph to hυ axis at the $(\alpha h\upsilon)^2 = 0$ determines the value of direct band gap.

equation that provides the correlation between α and E_g as below [45–47]:

$$(\alpha h\upsilon)^n = A(h\upsilon - E_g) \quad (2)$$

where A is proportionality constant, h is Planck's constant, υ is frequency of photon, and power n characterize type of electronic transition. $n = 1/2$ value corresponds to an indirect allowed transition. In Fig. 8, Tauc plots and estimated band gap values of various $Ni_{0.4}Cu_{0.2}Zn_{0.4}Tb_xFe_{2-x}O_4$ (x = 0.00–0.10) NSFs are given. Fig. 7 includes $(\alpha h\upsilon)^2$ versus energy (hυ) graphs. Second power means ($n = 2$) transitions are direct and allowed. Average E_g values are estimated from the intercept of linear portion of plots on energy axis. Mixed but undoped sample, $Ni_{0.4}Cu_{0.2}Zn_{0.4}Fe_2O_4$ has 1.87 eV band gap. Tb^{3+} ion doping process with the ratios of x = 0.00–0.10 do not cause much deviation from this magnitude. Most remarkable change is observed from sample $Ni_{0.4}Cu_{0.2}Zn_{0.4}Tb_{0.02}Fe_{1.98}O_4$ NSFs as equal to 1.98 eV band gap value [48,49]. All other substituted samples have E_g magnitudes between 1.87 and 1.98 eV [50]. There are reported E_g data for pristine, unsubstituted and substituted nanoferrites including Co, Ni, Mn elements [51–53]. Those literatures reported the E_g values within the range 1.46–3.86 eV. Among them, reported data by Quinonez et al. [51] are in good agreement with our E_g results.

3.5. Mössbauer study

Mössbauer spectra of $Ni_{0.4}Cu_{0.2}Zn_{0.4}Tb_xFe_{2-x}O_4$ ($0.00 \le x \le 0.1$) NSFs has been depicted in Fig. 9. The spectra were fitted using four sextets, A for T_d sites and B_1, B_2 and B_3 for O_h sites. The fitted parameters are presented in Table 2. For x = 0.08 and 0.1 substitutions, a small superparamagnetic doublet also designed additional to magnetic Zeeman sextets in samples. The Mössbauer parameters indicated this doublet is due to γ-Fe_2O_3 phase [54,55]. Generally, B-sites hyperfine

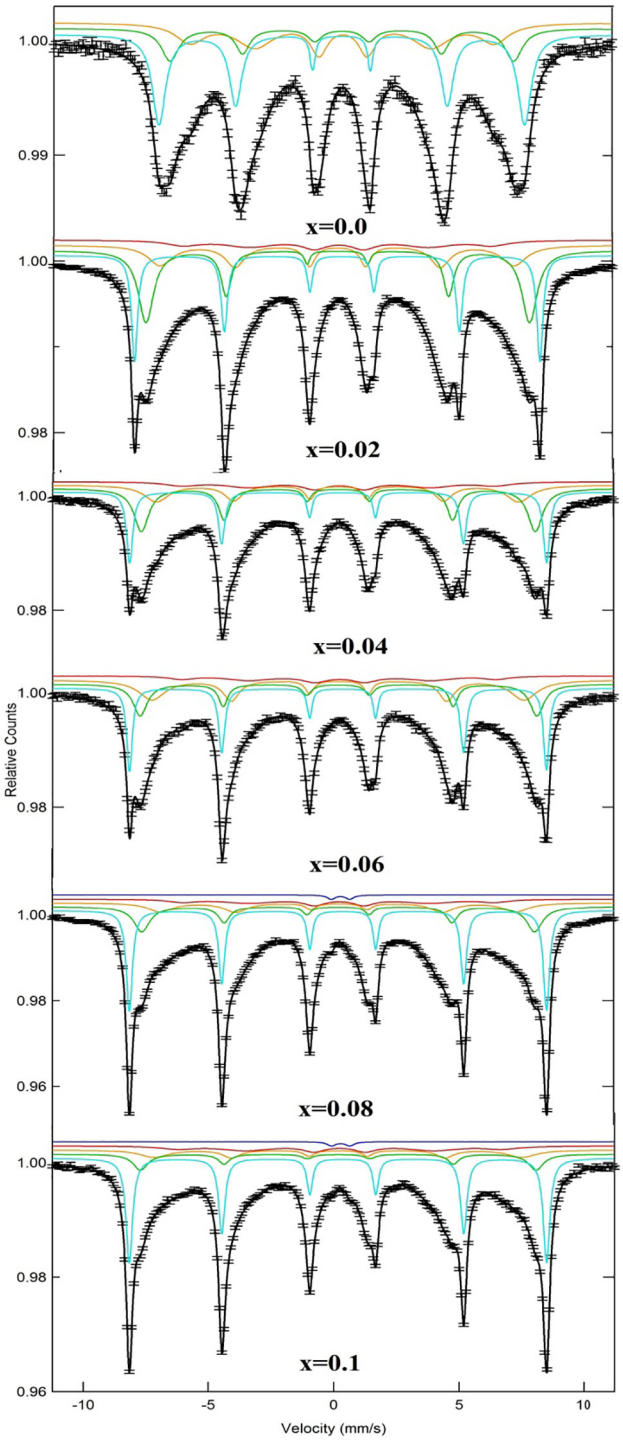

Fig. 9. Room Temperature Mössbauer spectra of $Ni_{0.4}Cu_{0.2}Zn_{0.4}Tb_xFe_{2-x}O_4$ (x = 0.00–0.10) NSFs.

magnetic field is greater than that of A-site, which was ascribed to the resulting dipolar field because of the deviation from cubic symmetry and covalent nature of T_d bonds [56]. As a result of the change in differing chemical environments and nuclear radius, the chemical isomer shift is occurring. The isomer shift values are changing between 0.284 and 0.372 mm/s which are characteristics of the high Fe^{3+} spins [57]. When the substitution is increased, the isomer shift of A and B sites fluctuates more. This shows the s electron density of Fe^{3+} ions are affected by substitution. The quadrupole splitting (Q.S) occurs due to chemical disorder in the material which results in an electric field gradient [56]. With respect to substitution, the Q.S values of B sites are negligible. This shows that the cubic symmetry of Oxygen ions around Fe^{3+} ions is not affected with substitution ions in the spinel structure. The relative areas of A and B sites indicate that the Ni ions occupied A and B sites. The large rare earth elements generally prefer B site, but the small ones occupy T_d [57,58]. T herefore the cation distribution of $Ni_{0.4}Cu_{0.2}Zn_{0.4}Tb_xFe_{2-x}O_4$ system was made using the formula $(Zn_{0.4}Ni_yFe_\lambda)^A(Ni_{0.4-y}Cu_{0.2}Tb_xFe_{2-\lambda-x})^B$. The estimated cation distribution from Mössbauer spectroscopy was given in Table 3. It showed that Fe^{3+} cations migrated from A site to B site with substitutions. The larger ions of Tb^{3+} (1.06 Å) prefer to O_h site.

Table 2
Parameters of Mössbauer Spectra of the $Ni_{0.4}Cu_{0.2}Zn_{0.4}Tb_xFe_{2-x}O_4$ (x = 0.00–0.10) NSFs (H_{hf}: hyperfine magnetic field. I.S: isomer shift. Q.S: quadrupole splitting. R_A: Relative area).

x	Spectral Component	I.S. (± 0.001) (mm s^{-1})	Q.S. (± 0.005) (mm s^{-1})	H_{hf} (± 0.01) (T)	Area (%)
0	Sx-A: Fe^{+3}	0.277	0.013	45.212	19.489
	Sx-B_1: Fe^{+3}	0.291	−0.09	42.486	25.434
	Sx-B_2: Fe^{+3}	0.318	−0.027	37.616	55.077
0.02	Sx-B_1: Fe^{+3}	0.372	−0.192	51.733	16.427
	Sx-A: Fe^{+3}	0.294	0.007	48.862	24.992
	Sx-B_2: Fe^{+3}	0.295	−0.021	44.823	28.14
	Sx-B_3: Fe^{+3}	0.331	−0.04	38.24	30.441
0.04	Sx-B_1: Fe^{+3}	0.371	−0.172	51.634	13.805
	Sx-A: Fe^{+3}	0.292	0	48.798	24.71
	Sx-B_2: Fe^{+3}	0.288	−0.032	44.866	24.235
	Sx-B_3: Fe^{+3}	0.311	−0.038	38.657	37.25
0.06	Sx-B_1: Fe^{+3}	0.371	−0.184	51.639	16.722
	Sx-A: Fe^{+3}	0.294	0.015	49.148	23.847
	Sx-B_2: Fe^{+3}	0.3	−0.033	46.057	27.039
	Sx-B_3: Fe^{+3}	0.337	−0.029	38.927	32.391
0.08	Sx-B_1: Fe^{+3}	0.372	−0.191	51.674	27.264
	Sx-A: Fe^{+3}	0.284	0.004	48.665	19.889
	Sx-B_2: Fe^{+3}	0.302	−0.033	44.05	20.836
	Sx-B_3: Fe^{+3}	0.321	−0.019	38.583	31.089
	Db: γ-Fe_2O_3	0.383	0.736	–	0.9218
0.1	Sx-B_1: Fe^{+3}	0.372	−0.192	51.682	31.373
	Sx-A: Fe^{+3}	0.301	−0.018	48.99	16.921
	Sx-B_2: Fe^{+3}	0.288	−0.013	45.596	17.274
	Sx-B_3: Fe^{+3}	0.349	0.012	40.092	33.291
	Db: γ-Fe_2O_3	0.387	0.724	–	1.1416

Table 3
Cation distribution of $Ni_{0.4}Cu_{0.2}Zn_{0.4}Tb_xFe_{2-x}O_4$ (x = 0.00–0.10) NSFs.

x	Tetrahedral (A-site)	Octahedral (B-site)
0.00	$Zn_{0.4}Ni_{0.08}Fe_{0.45}$	$Ni_{0.32}Cu_{0.2}Fe_{1.55}$
0.02	$Zn_{0.4}Ni_{0.1}Fe_{0.50}$	$Ni_{0.3}Cu_{0.2}Tb_{0.02}Fe_{1.48}$
0.04	$Zn_{0.4}Ni_{0.11}Fe_{0.49}$	$Ni_{0.29}Cu_{0.2}Tb_{0.04}Fe_{1.47}$
0.06	$Zn_{0.4}Ni_{0.14}Fe_{0.46}$	$Ni_{0.26}Cu_{0.2}Tb_{0.06}Fe_{1.48}$
0.08	$Zn_{0.4}Ni_{0.21}Fe_{0.39}$	$Ni_{0.19}Cu_{0.2}Tb_{0.08}Fe_{1.53}$
0.10	$Zn_{0.4}$ $Ni_{0.27}Fe_{0.33}$	$Ni_{0.13}Cu_{0.2}Tb_{0.1}Fe_{1.57}$

3.6. Magnetization

Magnetic traits of Tb substituted NiCuZn ferrites nanoparticles were evaluated using VSM. The experiments of magnetization against applied magnetic field (M-H) of $Ni_{0.4}Cu_{0.2}Zn_{0.4}Tb_xFe_{2-x}O_4$ ($0.00 \le x \le 0.10$) were performed at RT and at 10 K over the field range of +70 kOe to −70 kOe. The results of magnetic hysteresis loops of all products are presented in Fig. 10. From this figure, the magnitudes of M_s, H_c and M_r were deduced and listed in Table 4. It is noticed that the various $Ni_{0.4}Cu_{0.2}Zn_{0.4}Tb_xFe_{2-x}O_4$ ferrite nanoparticles show superparamagnetic (SPM) behavior at RT (Fig. 10(a) and (b)). However, the magnetization curve at 10 K (Fig. 10(a) and (b)) illustrates

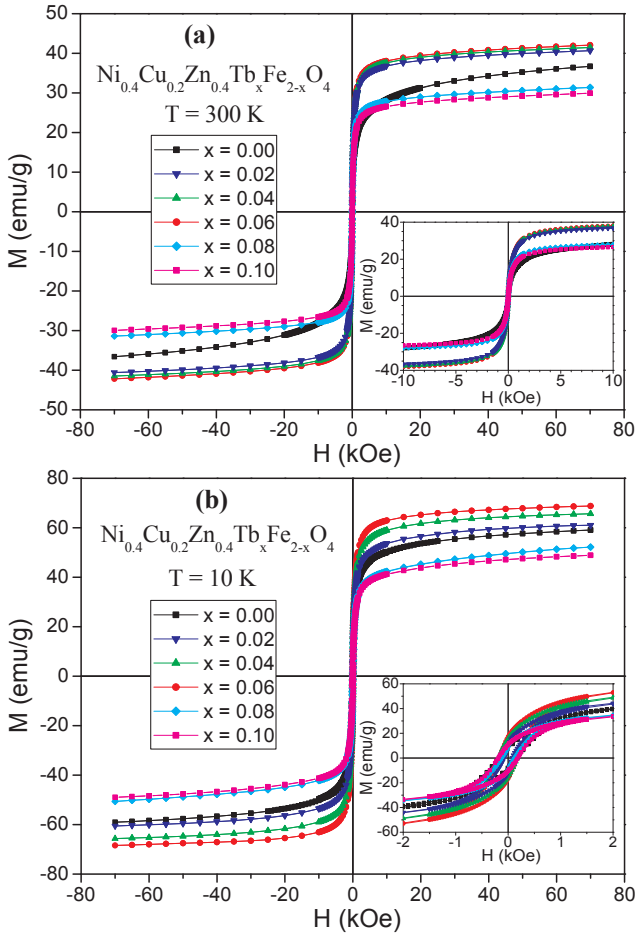

Fig. 10. M-H hysteresis loops of $Ni_{0.4}Cu_{0.2}Zn_{0.4}Tb_xFe_{2-x}O_4$ ($0.00 \le x \le 0.10$) NSFs performed at **(a)** T = 300 and **(b)** T = 10 K. The insets showed enlarged views near the coercivity.

typical character of soft ferromagnetic (FM) nanomaterials characterized by closed hysteresis loops with M_s, M_r and H_c. It is noticed that M_s of all produced nanoparticles are greater at low temperature than that of RT. For pure $Ni_{0.4}Cu_{0.2}Zn_{0.4}Fe_2O_4$ (x = 0.00) ferrite, M_s magnitude increases from 36.9 emu/g at RT to 59.3 emu/g at 10 K. The increase in M_s at 10 K compared with RT is ascribed to reduction of the thermal fluctuations and surface spins disorders at the surfaces of nanoparticles [59–61]. Indeed, the surface spins at high temperatures could be subjected in a short time to many disorder states with similar energies that lead to weaken their responses to the applied field and consequently decreases the magnetization in comparison to their bulk counterpart. Nevertheless, the surface spins can freeze to a certain state below the freezing/blocking temperature, which rises the projection of the moments in the direction of H. Moreover, the coercivity values of all the products increased at 10 K when compared with 300 K. The enhancement in H_c is ascribed to reduced thermal fluctuations energy at low temperatures that is less efficient in decreasing the effects of magneto-crystalline anisotropy energy.

The pure NiCuZn NSFs displays the highest M_s magnitudes of 36.9 and 59.3 emu/g at 300 K and 10 K, respectively. These values are in good agreement with those reported in NiCuZn ferrites NPs produced by means of sol–gel auto-combustion process [62,63] and in NiCuZn thin films [64]. Compared to pure NiCuZn NSFs, it was observed that M_s magnitudes initially increase with rising Tb^{3+} substituting level up to x = 0.06 and, then diminish for further concentration. Theoretically, it is anticipated that the magnetization of Tb^{3+} substituted NiCuZn NSFs increases because of the large magnetic moment of the Tb^{3+} ions (9.8 μ_B). Therefore, the initial increase in M_s of substituted NiCuZn with $x \le 0.06$ is considered with the larger magnetic moment of Tb^{3+} (9.8 μ_B) ions compared to Fe^{3+} ions (5 μ_B) and their preferential distributions in the octahedral lattice. In the case of $x > 0.06$, the magnetizations at both RT and 10 K do not survey the theoretical increase trend indicating a lattice distortion [65]. This may be ascribed to the screening of Tb^{3+} magnetic contributions by the influence of smaller crystallites as a result of Tb^{3+} inclusion [65]. This result further implies that the impact of size has a significant role in magnetic traits of higher Tb^{3+} content ($x > 0.06$) substituted NiCuZn NSFs. Usually, the reduction in magnetization is ascribed to surface effects of magnetic NSFs owing to smaller crystallites size, which could be explained by assuming the occurrence of dead magnetic layers because of the surface spins disorders [65]. It is anticipated that the number of spins at the surfaces of different prepared ferrites increases as the crystallites size become smaller. In this work, the increase and then the decrease in M_s values is followed by an enlargement and then a reduction of the crystallites size with increasing Tb^{3+} concentration [26,66]. Furthermore, consistent with Neel's sublattice model, spinal ferrites exhibit three kinds of interactions among tetrahedral and octahedral sites, e.g. A–A, B–B and A–B [67,68]. A–B sublattice interaction is the strongest among these three interactions. The total magnetization of doped NiCuZn NSFs is the difference amongst the magnetization of B and A sites. Because of their larger ionic radii, rare earth ions largely reside in the B sites [66]. Accordingly, because of the higher substitution of Fe^{3+} with Tb^{3+}, M_s could decrease as a result of reduced exchange interactions among Fe^{3+}-O-Fe^{3+}, which are substituted with the weaker Fe^{3+}-O-Tb^{3+} interaction. The experimental magnetic moments n_B per unit formula in units of Bohr magneton were determined via the following expression [69,70]:

$$n_B = \frac{Moleculor\ weight \times M_s}{5585} \quad (3)$$

The deduced n_B values were listed in the Table 4. Compared to pure NiCuZn NSFs, n_B values initially increase with increasing Tb^{3+} substituting level up to x = 0.06 and, then diminish for further concentration ($x > 0.06$). A good agreement between n_B and M_s variation tendency was observed. The increase and then the decrease in n_B are owing to the circumstance that the magnetization of the B sites is strengthening for $x \le 0.06$ and then is weakening for $x > 0.06$. Hence, the A–B exchange interaction is strengthening and then weakening with

Table 4
Magnetic parameters of $Ni_{0.4}Cu_{0.2}Zn_{0.4}Tb_xFe_{2-x}O_4$ (x = 0.00–0.10) NSFs deduced from VSM measurements performed at 300 and 10 K.

x	M_s (emu/g)		M_r (emu/g)		$R = M_r/M_s$		H_c (Oe)		$n_B(\mu_B)$	
	300 K	10 K	300 K	10 K	300 K	10 K	300 K	10 K	300 K	10 K
0.00	36.9	59.3	0.6	4.1	0.016	0.069	12.7	167.6	1.57	2.53
0.02	40.7	61.1	4.0	10.8	0.098	0.177	50.4	175.9	1.75	2.63
0.04	41.5	65.7	4.6	16.1	0.111	0.245	51.3	188.1	1.80	2.85
0.06	42.1	68.8	5.1	17.7	0.121	0.257	56.7	193.9	1.84	3.01
0.08	31.4	52.2	3.7	9.4	0.118	0.180	48.4	124.4	1.38	2.30
0.10	29.9	48.9	3.5	8.9	0.117	0.182	44.7	73.1	1.33	2.17

Tb^{3+} substitution, which would then disrupt the structure of collinear spins in the NiCuZn NSFs systems at the B sites [65].

On the other hand, it is noticed from Table 4 that the coercivity of $Ni_{0.4}Cu_{0.2}Zn_{0.4}Tb_xFe_{2-x}O_4$ ferrite nanoparticles initially increases and then decreases with increasing x at both 300 and 10 K. Pure NiCuZn NSFs exhibit H_c values of 12.7 (at T = 300 K) and 167.7 Oe (at T = 10 K), which increase to the 56.7 (at T = 300 K) and 193.9 Oe (at T = 10 K) for $Ni_{0.4}Cu_{0.2}Zn_{0.4}Tb_{0.06}Fe_{1.94}O_4$ (i.e. x = 0.06) NSFs and then decrease to the 44.7 (at T = 300 K) and 73.1 Oe (at T = 10 K) for $Ni_{0.4}Cu_{0.2}Zn_{0.4}Tb_{0.1}Fe_{1.9}O_4$ (i.e. x = 0.10) NSFs. It is well-known that the H_c and M_s are related by the following expression [71]:

$$H_c = \frac{2K}{\mu_0 M_s} \quad (4)$$

where K is magneto-crystalline anisotropy constant, and μ_0 is permeability of free space. Since M_s was found to increase and then decrease with x, the observed initial increase in coercivity could be a result of the strengthening of the magneto-crystalline anisotropy with $x \leq 0.06$ and then the weakening of the magneto-crystalline anisotropy with $x > 0.06$. Moreover, it is known that H_c is proportional to the grains size. In this study, it is observed that the crystallites size increases for lower Tb^{3+} amount and then reduces with further rising Tb^{3+} content. The coercivity shows comparable variation tendency of crystallites size. The values of squareness ratio "*R*" are also calculated and listed in Table 4. Commonly, the nanoparticles are considered to be in multi-magnetic domain (MMD) and in single magnetic domain (SMD) when $R \geq 0.5$ and $R < 0.5$, respectively [27,72]. The observed *R* values reflect the MMD nature in the different spinel ferrites nanoparticles.

4. Conclusion

$Ni_{0.4}Cu_{0.2}Zn_{0.4}Tb_xFe_{2-x}O_4$ (x = 0.00–0.10) NSFs were produced by ultrasonication technique. The formation of compositions is verified through XRD, FT-IR, SEM and TEM investigations. The lattice constant 'a' decreased with increasing Tb. The crystallites size is in range of 12–19 nm. DR % graphs revealed that the assessed direct and allowed E_g values lie between 1.87 and 1.98 eV bandgap range for all products. The Tb^{3+} substitution slightly changes the E_g magnitudes. The magnetic properties of various nanoparticles were analyzed at T = 300 K and 10 K. All prepared nanoparticles exhibit SPM nature at RT and soft ferromagnetic trait at 10 K. The deduced magnetic parameters of all the produced nanoparticles are increased with reducing the temperature from 300 to 10 K, which is due to reduction of the thermal fluctuations and surface spins disorders at the surfaces of nanoparticles. It is noticed that the M_s and M_r initially increase with increasing Tb^{3+} substituting level up to x = 0.06 and, then reduce for further concentration. The initial enhancement in magnetization of substituted NiCuZn NSFs with $x \leq 0.06$ is considered with the larger magnetic moment of Tb^{3+} (9.8 μ_B) ions compared to Fe^{3+} ions (5 μ_B) and their preferential distributions in the octahedral lattice, the increase in crystallites size and the strengthening of A-B exchange interaction. In the case of $x > 0.06$, the reduction in magnetizations is accredited to the lattice distortion, the screening of Tb^{3+} magnetic contributions by the influence of smaller crystallites, the reduction in crystallites size and weakening of A-B exchange interaction. The obtained squareness ratio $R < 0.5$ values reflect the MMD nature at both RT and 10 K in the different prepared spinel ferrites nanoparticles.

References

[1] E. Hema, A. Manikandan, M. Gayathri, M. Durka, S. Arul Antony, B.R. Venkatraman, The role of Mn^{2+}-doping on structural, morphological, optical, magnetic and catalytic properties of spinel $ZnFe_2O_4$ nanoparticles, J. Nanosci. Nanotechnol. 16 (2016) 5929–5943.

[2] A. Manikandan, A. Saravanan, S. Arul Antony, M. Bououdina, One-pot low temperature synthesis and characterization studies of nanocrystalline α-Fe_2O_3 based dye sensitized solar cells, J. Nanosci. Nanotechnol. 15 (2015) 4358–4366.

[3] A. Silambarasu, A. Manikandan, K. Balakrishnan, Room-temperature superparamagnetism and enhanced photocatalytic activity of magnetically reusable spinel ZnFe2O4 nanocatalysts, J. Supercond. Novel Magn. 30 (2017) 2631–2640.

[4] A. Silambarasu, A. Manikandan, K. Balakrishnan, S. Kumar Jaganathan, E. Manikandan, J. Sundeep Aanand, Comparative study of structural, morphological, magneto-optical and photo-catalytic properties of magnetically reusable spinel $MnFe_2O_4$ nano-catalysts, J. Nanosci. Nanotechnol. 18 (2018) 3523–3531.

[5] G.D. Nipan, V.A. Ketsko, A.I. Stognij, A.V. Trukhanov, T.N. Koltsova, M.A. Kopeva, L.V. Elesina, N.T. Kuznetsov, Properties of $Mg(Fe_{1-x}Ga_x)_2O_{4+\delta}$ solid solutions in stable and metastable states, Inorg. Mater. 46 (2010) 429–433.

[6] G. Satyanarayana, G.N. Rao, K.V. Babu, Structural, dielectric and magnetic properties of Al^{3+} and Cr^{3+} substituted Ni-Zn-Cu ferrites, J. Nanosci. Tech. 487 (2018) 487–491.

[7] N. Sanpo, C.C. Berndt, C. Wen, J. Wang, Transition metal-substituted cobalt ferrite nanoparticles for biomedical applications, Acta Biomater. 9 (2013) 5830–5837.

[8] T. Ahmad, H. Bae, Y. Iqbal, I. Rhee, S. Hong, Y. Chang, et al., Chitosan-coated nickel-ferrite nanoparticles as contrast agents in magnetic resonance imaging, J. Magn. Magn. Mater. 318 (2015) 151–157.

[9] M. Ansari, A. Bigham, S.A. Hassanzadeh-Tabrizi, H. Abbastabar Ahangar, Synthesis and characterization of $Cu_{0.3}Zn_{0.5}Mg_{0.2}Fe_2O_4$ nanoparticles as a magnetic drug delivery system, J. Magn. Magn. Mater. 439 (2017) 67–75.

[10] G. Wang, F. Zhou, X. Li, J. Li, Y. Ma, J. Mu, et al., Controlled synthesis of L-cysteine coated cobalt ferrite nanoparticles for drug delivery, Ceram. Int. 44 (2018) 13588–13594.

[11] P. Chen, B. Cui, Y. Bu, Z. Yang, Y. Wang, Synthesis and characterization of mesoporous and hollow-mesoporous MxFe3-xO4 (M = Mg, Mn, Fe Co, Ni, Cu, Zn) microspheres for microwave-triggered controllable drug delivery, J. Nano Res. 19 (2017) 398.

[12] A. Hanini, L. Lartigue, J. Gavard, K. Kacem, C. Wilhelm, F. Gazeau, et al., Zinc substituted ferrite nanoparticles with $Zn_{0.9}Fe_{2.1}O_4$ formula used as heating agents for in vitro hyperthermia assay on glioma cells, J. Magn. Magn. Mater. 416 (2016) 315–320.

[13] Vanessa Pilati, Rafael Cabreira Gomes, Guilherme Gomide, Priscilla Coppola, Franciscarlos G. Silva, Fábio L.O. Paula, Régine Perzynski, Gerardo F. Goya, Renata Aquino, Jérôme Depeyrot, Core/shell nanoparticles of non-stoichiometric Zn–Mn and Zn–Co ferrites as thermosensitive heat sources for magnetic fluid hyperthermia, J. Phys. Chem. C 122 (5) (2018) 3028–3038, https://doi.org/10.1021/acs.jpcc.7b11014.

[14] E. Skliri, J. Miao, J. Xie, G. Liu, T. Salim, B. Liu, et al., Assembly and photochemical properties of mesoporous networks of spinel ferrite nanoparticles for environmental photocatalytic remediation, Appl. Catal. B: Environ. 227 (2018) 330–339.

[15] A.F.S. Abu-Hani, S.T. Mahmoud, F. Awwad, A.I. Ayesh, Design, fabrication, and characterization of portable gas sensors based on spinel ferrite nanoparticles embedded in organic membranes, Sens. Actuators B Chem. 241 (2017) 1179–1187.

[16] K.B.N. Chandra, W. Madhuri, Microwave processed bulk and nano NiMg ferrites: a comparative study on X-band electromagnetic interference shielding properties, Mater. Chem. Phys. 187 (2017) 164–176.

[17] S.R. Bhongale, H.R. Ingavale, T.J. Shinde, P.N. Vasambekar, Microwave sintered Mg-Cd ferrite substrates for microstrip patch antennas in X-band, AEU – Int. J. Electron. Comm. 96 (2018) 246–251.

[18] A. Geiler, V. Harris, Atom magnetism: ferrite circulators-Past, present, and future, IEEE Microwave Mag. 15 (2014) 66–72.

[19] V.G. Harris, Modern microwave ferrites, IEEE Trans. Magn. 48 (2012) 1075–1104.

[20] S. Patange, S.E. Shirsath, K. Lohar, S. Algude, S. Kamble, N. Kulkarni, et al., Infrared spectral and elastic moduli study of $NiFe_{2-x}Cr_xO_4$ nanocrystalline ferrites, J. Magn. Magn. Mater. 325 (2013) 107–111.

[21] M.N. Akhtar, M.A. Khan, M.R. Raza, M. Ahmad, G. Murtaza, R. Raza, et al., Structural morphological, dielectric and magnetic characterizations of $Ni_{0.6}Cu_{0.2}Zn_{0.2}Fe_2O_4$ (NCZF/MWCNTs/PVDF) nanocomposites for multilayer chip inductor (MLCI) applications, Ceram. Int. 40 (2014) 15821–15829.

[22] K. Elayakumar, A. Dinesh, A. Manikandan, Murugesan Palanivelu, G. Kavitha, F.S. Prakash, R. Thilak Kumar, Saravana Kumar Jaganathan, A. Baykal, Structural morphological, enhanced magnetic properties and antibacterial bio-medical activity of rare earth element (REE) cerium (Ce^{3+}) doped $CoFe_2O_4$ nanoparticles, J. Magn. Magn. Mater. 476 (2019) 157–165.

[23] K. Elayakumar, A. Manikandan, A. Dinesh, K. Thanrasu, K. Kanmani Raja, R. Thilak Kumar, Y. Slimani, S.K. Jaganathan, A. Baykal, Enhanced magnetic property and antibacterial biomedical activity of Ce^{3+} doped $CuFe_2O_4$ spinel nanoparticles synthesized by sol-gel method, J. Magn. Magn. Mater. 478 (2019) 140–147.

[24] Y. Slimani, M.A. Almessiere, M. Nawaz, A. Baykal, S. Akhtar, I. Ercan, et al., Effect of bimetallic (Ca, Mg) substitution on magneto-optical properties of $NiFe_2O_4$ nanoparticles, Ceram. Int. 45 (2019) 6021–6029.

[25] S. Singhal, J. Singh, S. Barthwal, K. Chandra, Preparation and characterization of nanosize nickel-substituted cobalt ferrites ($Co_{1-x}Ni_xFe_2O_4$), J. Solid State Chem. 178 (2005) 3183–3189.

[26] M. Almessiere, Y. Slimani, S. Güner, A. Baykal, I. Ercan, Effect of dysprosium substitution on magnetic and structural properties of $NiFe_2O_4$ nanoparticles, J. Rare Earths 37 (2019) 871–878.

[27] M.A. Almessiere, Y. Slimani, S. Guner, M. Sertkol, A.D. Korkmaz, Sagar E. Shirsath, A. Baykal, Sonochemical synthesis and physical properties of $Co_{0.3}Ni_{0.5}Mn_{0.2}Eu_xFe_{2-x}O_4$ nano-spinel ferrites, Ultrason. Sonochem. 58 (2019) 104654.

[28] M. Almessiere, A. Demir Korkmaz, Y. Slimani, M. Nawaz, S. Ali, A. Baykal, Magneto-optical properties of rare earth metals substituted Co-Zn spinel nanoferrites, Ceram. Int. 45 (2019) 3449–3458.

[29] M. Almessiere, Y. Slimani, A. Korkmaz, S. Guner, M. Sertkol, S.E. Shirsath, et al., Structural, optical and magnetic properties of Tm^{3+} substituted cobalt spinel ferrites synthesized via sonochemical approach, Ultrason. Sonochem. 54 (2019) 1–10.

[30] K. Lohar, A. Pachpinde, M. Langade, R. Kadam, S.E. Shirsath, Self-propagating high temperature synthesis, structural morphology and magnetic interactions in rare earth Ho^{3+} doped $CoFe_2O_4$ nanoparticles, J. Alloy. Compd. 604 (2014) 204–210.

[31] S.M. Kabbur, S.D. Waghmare, D.Y. Nadargi, S.D. Sartale, R.C. Kambale, U.R. Ghodake, et al., Magnetic interactions and electrical properties of Tb^{3+} substituted NiCuZn ferrites, J. Magn. Magn. Mater. 473 (2019) 99–108.

[32] V. Mary Teresita, A. Manikandan, B. Avila Josephine, S. Sujatha, Electromagnetic properties and humidity-sensing studies of magnetically recoverable $LaMg_xFe_{1-x}O_{3-\delta}$ perovskites nano-photocatalysts by sol-gel route, J. Supercond. Novel Magn. 29 (2016) 1691–1701.

[33] M.A. Gabal, Y.M. Al Angari, A.Y. Obaid, A. Qusti, Structural analysis and magnetic properties of nanocrystalline NiCuZn ferrites synthesized via a novel gelatin method, Adv. Powder Tech. 25 (2014) 457–461.

[34] M. Penchal Reddy, G. Balakrishnaiah, W. Madhuri, M.V. Ramana, N.R. Reddy, K.V.S. Kumar, et al., Structural magnetic and electrical properties of NiCuZn ferrites prepared by microwave sintering method suitable for MLCI applications, J. Phys. Chem. Solids 71 (2010) 1373–1380.

[35] M.A. Gabal, A.M. Asiri, Y.M. AlAngari, On the structural and magnetic properties of La-substituted NiCuZn ferrites prepared using egg-white, Ceram. Int. 37 (2011) 2625–2630.

[36] J.J. Shrotri, S.D. Kulkarni, C.E. Deshpande, A. Mitra, S.R. Sainkar, P.S.A. Kumar, et al., Effect of Cu substitution on the magnetic and electrical properties of Ni–Zn ferrite synthesized by soft chemical method, Mater. Chem. Phys. 59 (1999) 1–5.

[37] H.I. Hsiang, J.L. Wu, Copper-rich phase segregation effects on the magnetic properties and DC-bias-superposition characteristic of NiCuZn ferrites, J. Magn. Magn. Mater. 374 (2015) 367–371.

[38] H. Harzali, A. Marzouki, F. Saida, A. Megriche, A. Mgaidi, Structural magnetic and optical properties of nanosized $Ni_{0.4}Cu_{0.2}Zn_{0.4}R_{0.05}Fe_{1.95}O_4$ (R = Eu^{3+}, Sm^{3+}, Gd^{3+} and Pr^{3+}) ferrites synthesized by co-precipitation method with ultrasound irradiation, J. Magn. Magn. Mater. 460 (2018) 89–94.

[39] H. Harzali, F. Saida, A. Marzouki, A. Megriche, F. Baillon, F. Espitalier, Structural and magnetic properties of nano-sized NiCuZn ferrites synthesized by co-precipitation method with ultrasound irradiation, J. Magn. Magn. Mater. 419 (2016) 50–56.

[40] C. Barathiraja, A. Manikandan, A.M. Uduman Mohideen, Magnetically recyclable spinel $Mn_xNi_{1-x}Fe_2O_4$(x = 0.0–0.5) nano-photocatalysts: structural, morphological and opto-magnetic properties, J. Supercond. Novel Magn. 29 (2016) 477–486.

[41] A. Manikandan, S. Arul Antony, R. Sridhar, S. Ramakrishna, M. Bououdina, A simple combustion synthesis and optical studies of magnetic $Zn_{1-x}Ni_xFe_2O_4$ nanostructures for photoelectrochemical applications, J. Nanosci. Nanotechnol. 15 (2015) 4948–4960.

[42] M.H. Abdellatifa, A.A. Azaba, M. Salerno, Effect of rare earth doping on the vibrational spectra of spinel Mn-Cr ferrite, Mater. Res. Bull. 97 (2018) 260–264.

[43] K.V. Zipare, S.S. Bandgar, G.S. Shahane, Effect of Dy-substitution on structural and magnetic properties of MnZn ferrite nanoparticles, J. Rare Earths 36 (2018) 86–94.

[44] M.M. Baig, M.A. Yousuf, M.F. Warsi, P.O. Agboola, M. Sher, I. Shakir, Ceram. Int. (2019), https://doi.org/10.1016/j.ceramint.2019.06.020.

[45] J. Tauc, R. Grigorovici, A. Vancu, Optical properties and electronic structure of amorphous germanium, Physica Status Solidi 15 (1966) 627–637.

[46] A. Baykal, S. Esir, A. Demir, S. Güner, Magnetic and optical properties of $Cu_{1-x}Zn_xFe_2O_4$ nanoparticles dispersed in a silica matrix by a sol-gel auto-combustion method, Ceram. Int. 41 (2015) 231–239.

[47] A. Baykal, S. Güner, A. Demir, S. Esir, F. Genç, Effects of Zinc substitution on magneto-optical properties of $Mn_{1-x}Zn_xFe_2O_4/SiO_2$ nanocomposites, Ceram. Int. 40 (2014) 13401–13408.

[48] M.F. Valan, A. Manikandan, S. Arul Antony, Microwave combustion synthesis and characterization studies of magnetic $Zn_{1-x}Cd_xFe_2O_4$ ($0 \le x \le 0.5$) nanoparticles, J. Nanosci. Nanotechnol. 15 (2015) 4543–4551.

[49] G. Padmapriya, A. Manikandan, V. Krishnasamy, Saravana Kumar Jaganathan, S. Arul Antony, Enhanced catalytic activity and magnetic properties of spinel $MnxZn_{1-x}Fe_2O_4$ ($0.0 \le x \le 1.0$) nano-photocatalysts by microwave irradiation route, J. Supercond. Novel Magn. 29 (2016) 2141–2149.

[50] A. Manikandan, M. Durka, S. Arul Antony, Magnetically recyclable spinel $Mn_xZn_{1-x}Fe_2O_4$ ($0.0 \le x \le 0.5$) nano-photocatalysts, Adv. Sci. Eng. Med. 7 (2015) 33–46.

[51] J.L.O. Quinonez, U. Pal, M.S. Villanueva, Structural, magnetic, and catalytic evaluation of spinel Co, Ni, and Co-Ni ferrite nanoparticles fabricated by low-temperature solution combustion process, ACS Omega 3 (2018) 14986–15001.

[52] E.C. Devi, I. Soibam, A low temperature synthesis and optical characterization on Mn-Ni mixed nanoferrites, Indian J. Sci. Tech. 10 (2017) 1–5.

[53] R.S. Melo, P. Banerjee, A. Franco Jr, Hydrothermal synthesis of nickel doped ferrite nanoparticles: optical and magnetic properties, J. Mater. Sci.: Mater. Electron. 29 (2018) 14657–14667.

[54] T. Liu, L. Guo, Y. Tao, Y.B. Wang, W.D. Wang, Synthesis and interfacial structure of nanoparticles γ-Fe_2O_3 coated with surfactant DBS and CTAB, Nanostruct. Mater. 11 (1999) 487–492.

[55] R. Zboril, M. Mashlan, D. Petridis, D. Krausova, P. Pikal, The role of intermediates in the process of red ferric pigment manufacture from $FeSO_4{\cdot}7H_2O$, Hyperfine Interact. 139 (140) (2002) 437–445.

[56] A. Lakshman, P.S.V. Subba Rao, K.H. Rao, Mössbauer spectroscopic analyses of $Mg_{0.9}Cu_{0.1}Mn_{0.05}Cr_xFe_{1.95-x}O_4$ spinel ferrites, Mater. Lett. 60 (2006) 7–10.

[57] Y. Zhang, D. Wen, Infrared emission properties of RE (RE= La, Ce, Pr, Nd, Sm, Eu, Gd, Tb, and Dy) and Mn co-doped $Co_{0.6}Zn_{0.4}Fe_2O_4$ ferrites, Mater. Chem. Phys. 131 (2012) 575–580.

[58] S. Amiri, H. Shokrollahi, Magnetic and structural properties of RE doped Co-ferrite (RE=Nd, Eu, and Gd) nano-particles synthesized by co-precipitation, J. Magn. Magn. Mater. 345 (2013) 18–23.

[59] M.A. Almessiere, Y. Slimani, S. Güner, J. van Leusen, A. Baykal, P. Kögerler, Effect of Nb^{3+} ion substitution on the magnetic properties of $SrFe_{12}O_{19}$ hexaferrites, J. Mater. Sci.: Mater. Electron. 30 (12) (2019) 11181–11192.

[60] M.A. Almessiere, Y. Slimani, H. Gungunes, A. Manikandan, A. Baykal, Investigation of the effects of Tm^{3+} on the structural, microstructural, optical, and magnetic properties of Sr hexaferrites, Results Phys. 13 (2019) 102166.

[61] M.A. Almessiere, Y. Slimani, H.S. El Sayed, A. Baykal, Morphology and magnetic traits of strontium nanohexaferrites: effects of manganese/yttrium co-substitution, J. Rare Earths (2019), https://doi.org/10.1016/j.jre.2018.09.014.

[62] V. Chaudhari, Sagar E. Shirsath, M.L. Mane, R.H. Kadam, S.B. Shelke, D.R. Mane, Crystallographic magnetic and electrical properties of $Ni_{0.5}Cu_{0.25}Zn_{0.25}La_xFe_{2-x}O_4$ nanoparticles fabricated by sol–gel method, J. Alloy. Compd. 549 (2013) 213–220.

[63] P.K. Roy, J. Bera, Electromagnetic properties of samarium-substituted NiCuZn ferrite prepared by auto-combustion method, J. Magn. Magn. Mater. 321 (2009) 247–251.

[64] Feng Liu, Chen Yang, A.Z. Tianling Ren, Jun Yu Wang, Litian Liu, NiCuZn ferrite thin films grown by a sol–gel method and rapid thermal annealing, J. Magn. Magn. Mater. 309 (2007) 75–79.

[65] C. Murugesan, G. Chandrasekaran, Impact of Gd^{3+} substitution on the structural, magnetic and electrical properties of cobalt ferrite nanoparticles, RSC Adv. 5 (2015) 73714–73725.

[66] M.A. Almessiere, Y. Slimani, S. Güner, M. Nawaz, A. Baykal, F. Aldakheel, S. Akhtar, I. Ercan, İ. Belenli, B. Ozçelik, Magnetic and structural characterization of Nb^{3+}-substituted $CoFe_2O_4$ nanoparticles, Ceram. Int. 45 (2019) 8222–8232.

[67] M.A. Almessiere, Y. Slimani, S. Guner, M. Nawaz, A. Baykal, F. Aldakheel, A. Sadaqat, I. Ercan, Effect of Nb substitution on magneto-optical properties of $Co_{0.5}Mn_{0.5}Fe_2O_4$ nanoparticles, J. Mol. Struct. 1195 (2019) 269–279.

[68] M.A. Almessiere, Y. Slimani, M. Sertkol, F.A. Khan, M. Nawaz, H. Tombuloglu, E.A. Al-Suhaimi, A. Baykal, Ce–Nd Co-substituted nanospinel cobalt ferrites: an investigation of their structural, magnetic, optical, and apoptotic properties, Ceram. Int. 45 (2019) 16147–16156.

[69] M.A. Almessiere, Y. Slimani, U. Kurtan, S. Guner, M. Sertkol, Sagar E. Shirsath, S. Akhtar, A. Baykal, I. Ercan, Structural magnetic, optical properties and cation distribution of nanosized $Co_{0.7}Zn_{0.3}Tm_xFe_{2-x}O_4$ ($0.0 \le x \le 0.04$) spinel ferrites synthesized by ultrasonic irradiation, Ultrason. Sonochem. 58 (2019) 104638.

[70] M.A. Almessiere, Y. Slimani, A.D. Korkmaz, N. Taskhandi, M. Sertkol, A. Baykal, Sagar E. Shirsath, İ. Ercan, B. Ozçelik, Sonochemical synthesis of Eu^{3+} substituted $CoFe_2O_4$ nanoparticles and their structural, optical and magnetic properties, Ultrason. Sonochem. 58 (2019) 104621.

[71] M.A. Almessiere, Y. Slimani, M. Sertkol, M. Nawaz, A. Sadaqat, A. Baykal, I. Ercan, B. Ozçelik, Effect of Nb^{3+} substitution on the structural, magnetic, and optical properties of $Co_{0.5}Ni_{0.5}Fe_2O_4$ nanoparticles, Nanomaterials 9 (2019) 430.

[72] Y. Slimani, M.A. Almessiere, S. Güner, N.A. Tashkandi, A. Baykal, M.F. Sarac, M. Nawaz, I. Ercan, Calcination effect on the magneto-optical properties of Vanadium substituted $NiFe_2O_4$ nanoferrites, J. Mater. Sci.: Mater. Electron. 30 (2019) 9143–9154.